Chemical Science

Accepted Manuscript

This article can be cited before page numbers have been issued, to do this please use: S. Li, X. Jiang, Y. Fan, B. Liu, H. Zeng and G. Guo, *Chem. Sci.*, 2018, DOI: 10.1039/C8SC01210E.

ROYAL SOCIETY OF CHEMISTRY

rsc.li/chemical-science

View Article Online
DOI: 10.1039/C8SC01210E

Journal Name

ARTICLE

New Strategy for Designing Promising Mid-Infrared Nonlinear Optical Materials: Narrowing Band Gap for Large Nonlinear Optical Efficiency and Reducing Thermal Effect for High Laser-induced Damage Threshold

Received 00th January 20xx,
Accepted 00th January 20xx

DOI: 10.1039/x0xx00000x

www.rsc.org/

Shu-Fang Li,[a] Xiao-Ming Jiang,[a,*] Yu-Hang Fan,[b] Bin-Wen Liu,[a] Hui-Yi Zeng,[a] and Guo-Cong Guo[a,*]

To circumvent the incompatibility between large nonlinear optical (NLO) efficiency and high laser-induced damage threshold (LIDT) in mid-infrared NLO materials, a new strategy for designing both excellent properties is proposed. This strategy involves narrowing band gap for large NLO efficiency and reducing thermal effect for high LIDT. To support of these proposals, a series of isostructural chalcogenides with various tetrahedral center cations, $Na_2Ga_2MQ_6$ (M = Ge, Sn; Q = S, Se), were synthesized and studied in detail. Compared with the benchmark AGS, these chalcogenides exhibit significantly narrower band gaps (1.56–1.73 eV, AGS: 2.62 eV) and high NLO efficiencies (1.6–3.9 times that of AGS at 1910 nm), and also outstanding LIDTs of 8.5–13.3 × AGS for potential high-power applications, which are contrary to the conventional band gap view but can be attributed to their small thermal expansion anisotropy, surmounting the NLO-LIDT incompatibility. These results shed light on the exploration of practical IR NLO materials with excellent performance not restricted by the NLO–LIDT incompatibility.

Introduction

Nonlinear optical (NLO) materials are at the research front-lines of laser science and technology because of their ability to produce coherent and tunable light from solid-state lasers in the fields of medical, military and communication network.[1-4] For decades, various NLO materials such as β-BaB_2O_4 (BBO),[5] LiB_3O_5 (LBO),[6] KH_2PO_4 (KDP),[7] $KBe_2B_2O_6F_2$ (KBBF),[8] and $KTiOPO_4$ (KTP)[9] have been dis-covered and used commercially. Although these materials are applicable for generating of coherent light from the ultraviolet region to the near-infrared (IR) region, the direct generation of mid-IR (2-20 μm) coherent light by second harmonic generation (SHG) remains particularly challenging, but crucial to various communication and optoelectronic devices.[10] For decades, numerous mid-IR NLO materials with obvious SHG responses, mainly including pnictides, chalcogenides, and halogenides, have been report-ed.[11-12] However, only a few of them, namely, $AgGaS_2$ (AGS),[13-14] $AgGaSe_2$ (AGSe),[15-16] and $ZnGeP_2$ (ZGP),[17] can be used. Unfortunately, these materials suffer from defects such as low laser-induced damage thresholds (LIDT) that hinder their high-power applications.[11] Therefore, developing of new mid-IR NLO materials with excellent comprehensive performance (large NLO efficiency, high LIDT, wide transparency window, and sufficient birefringence to achieve phase matchability)[18] is technologically and scientifically important.

Among all the requirements for high-power applications, large NLO efficiency and high LIDT are the most challenging to achieve concurrently. Previous theoretical and experimental studies on IR NLO materials show that the wider band gaps are beneficial to high LIDTs,[1, 19-20] while also resulting in small NLO efficiency, which implies the incompatibility between large NLO efficiency and high LIDT. Two main methods have been adopted to balance the conflict. One is increasing the band gap by replacing the Ag^+ in classical IA-IIIA-VIA_2 type of IR NLO materials with strong electropositive alkali or alkaline-earth metal. Thus, $LiBQ_2$ (B = Ga, In; Q = S, Se, Te) family and $BaGa_4S_7$ were observed,[21-25] their band gaps up to 4 eV lead to LIDTs exceeding those of the Ag analogs, while their NLO efficiencies are slightly lower. For example, the band gap of $LiGaS_2$ is 3.65 eV, which is significantly larger than that of AGS (2.62 eV);[26] nevertheless, the SHG coefficient of $LiGaS_2$ is approximately a quarter of that of AGS.[27] The other method involves combing two or more NLO-active motifs such as GaQ_4, InQ_4, GeQ_4, and SiQ_4 (Q = S, Se) tetrahedra in a single IR NLO chalcogenide compound to modulate the LIDT and NLO efficiency.[28-44] The combination of different NLO-active motifs can optimize the NLO efficiency and LIDT with high flexibility. For example, by incorporating GeS_2 into $AgGaS_2$, quaternary $AgGaGeS_4$ was developed with improved LIDT, which makes it a promising

[a] State Key Laboratory of Structural Chemistry, Fujian Institute of Research on the Structure of Matter, Chinese Academy of Sciences, Fuzhou, Fujian 350002, P.R. China.
[b] School of Chemistry and Chemical Engineering, Yangtze Normal University.
E-mail: gcguo@fjirsm.ac.cn; xmjiang@fjirsm.ac.cn
Electronic Supplementary Information (ESI) available: CSD 432399, 432400, 432402, 432403. For ESI and crystallographic data in CIF or other electronic format see DOI: 10.1039/x0xx00000x

View Article Online
DOI: 10.1039/C8SC01210E

alternative to the widely used AGS.[45-47] Additionally, a series of Li-containing quaternary compounds have been reported, including $Li_2Ga_2GeS_6$, $LiGaGe_2Se_6$, $Li_2In_2GeSe_6$, and $Li_2In_2SiSe_6$, the combination of different microscopic NLO-active units, namely, GaQ_4, InQ_4, GeQ_4, SiQ_4, in these compounds strengthen their nonlinear susceptibilities compared with the corresponding ternary compounds.[21, 48-49] Although many attempts have been made using these two main methods, excellent IR NLO materials with both high LIDT and strong NLO efficiency are rare.

Theoretically, SHG is a two-photon process, and the value of NLO efficiency is determined by the optical transition matrix elements, which strongly depend on the band gap of an IR NLO material.[50] Normally, a small band gap can easily result in strong optical transition and is therefore beneficial to large NLO efficiency. Compared with SHG, the laser damage on the NLO crystals is a highly complicated process that involves pitting, erosion, melting, delamination, fracture, and discoloration.[51] The mechanisms of laser damage process can be mainly categorized into thermal processes and dielectric processes. For NLO crystals with high laser transparency and few defects for optical absorption, dielectric process mechanism is applied, and dielectric LIDT is proportional to atomic density/(n^2-1), where n is refractivity and has large values for materials with narrow band gaps. Therefore, the narrow band gaps simultaneously lead to large NLO efficiency and low LIDT. This result is also the reason for the so-called incompatibility between large NLO efficiency and high LIDT in some NLO compound systems, such as well-known oxides and IA-IIIA-VIA_2 type of IR NLO materials.[7]

However, for many practical mid-IR NLO materials, intrinsic and defect-induced optical absorptions are non-negligible, which may lead to a temperature increase when the laser beam is incident on the surface of an NLO crystal, thereby resulting in thermal expansion, strain, distortion, cracking, catastrophic shattering and so on. In this condition, the thermal process mechanism can be applied;[51] corresponding thermal LIDTs scale proportionally to $C\kappa S/\alpha\beta$, where C is the heat capacity of the material and can seem close to each other for any solid with a similar atomic density above room temperature, κ is thermal conductivity, S is damaging stress and is positively correlated with Young's modulus and shear modulus of the material, β is expansion coefficient and α is absorption coefficient. These results show that LIDT can be enhanced by reducing the thermal effects, i.e., by increasing the thermal conductivity and damaging stress, and decreasing the expansion and absorption coefficients of the IR NLO materials.

The intrinsic physical parameters of NLO crystals, thermal conductivity, damaging stress, and absorption coefficient strongly depend on the microscopic structural features of practical crystals, such as number and size of localized absorbing defects and impurities.[52-54] Nevertheless, the expansion coefficient of a particular type of NLO crystal does not change significantly with different crystal growing conditions. Therefore, from the perspective of crystal structural design of mid-IR NLO materials, the parameter of expansion coefficient may be modulated in a relatively easy manner to enhance LIDT. The expansion coefficient of a compound depends on the expansion coefficients (dR/dT) of all chemical bonds in it, which can be evaluated through $dR/dT = 1.35k/G$ based on bond-valence theory,[55] where k is the Boltzmann constant and G is the force constant of the chemical bonds. Normally, for the same type of chemical bonds, G is larger for shorter bond lengths. However, for the same types of center and coordinated ions, according to the bond-valence-sum rule, center ions that have fewer coordinated atoms are likely to form shorter bond lengths and larger force constants. In such circumstances, relatively smaller thermal expansion coefficients and higher LIDT can be predicted.

For the case in which thermal LIDT dominates the laser-induced damage process in the practical application of mid-IR NLO materials, NLO efficiency and LIDT are relatively independent of each other, and almost no incompatibility exists between them. We propose the new strategy of designing IR NLO materials by narrowing the band gap for large NLO efficiency and reducing the thermal effect for high laser-induced damage threshold. These approaches are effective in achieving high NLO efficiency and LIDT concurrently.

Recently, metal chalcogenides are highly attractive in exploring new mid-IR NLO materials. Some alkali metal-contained quaternary chalcogenides were reported to exhibit large NLO efficiencies, such as $K_4GeP_4Se_{12}$,[56] $Na_2Ge_2Se_5$,[57] K_3TaAsS_{11},[10] and $CsZrPSe_6$,[58] which possess NLO coefficients of 14.02, 12.01, 9.91, and 9.92 times that of AGS, respectively. Highly electropositive alkali metals in these chalcogenides usually play the role of dimensional reduction agents to reduce the coordinated atoms of host chalcogenide frameworks. Based on the preceding analysis, besides having high NLO efficiencies, alkali-metal-contained chalcogenides may exhibit high LIDTs due to the strengthening of force constants and the reduction of thermal expansion coefficients of metal-chalcogen bonds.

To verify our new strategy, we found four new compounds in the alkali metal sodium-contained chalcogenides, namely, $Na_2Ga_2GeSSe_5$ (**1**), $Na_2Ga_2GeSe_6$ (**2**), $Na_2Ga_2SnSSe_5$ (**3**), and $Na_2Ga_2SnSe_6$ (**4**). All these materials exhibit phase-matching behavior with large NLO efficiency of 1.6–3.9 × AGS. Their band gaps are obviously narrower than those of AGS, which should result in relatively smaller LIDTs based on the conventional view. However, the four compounds exhibit extremely large LIDTs of 8.5–13.3 × AGS, which can be attributed to their smaller thermal expansion anisotropy compared with those of AGS. In the following section, we report synthesis, characterization, optical and thermal properties of these compounds. Theoretical calculations of electronic band structures and NLO efficiencies are also conducted for these compounds.

View Article Online
DOI: 10.1039/C8SC01210E

Experimental Section

Synthesis. The chemicals used in this study are the following: Na (99.7%), Ga (99.99%), Ge (99.99%), Sn (99.9%), S (99.5%), and Se (99.9%). All of these chemicals were from Aladdin Chemistry Co. Ltd. and were used as received without further purification. Na_2S and Na_2Se starting materials were prepared through stoichiometric reaction of Na and S or Se in liquid ammonia.[30] For the synthesis of target compounds, a stoichiometric mixture of starting materials Na_2S, Ga, Ge (Sn), and Se in a molar ratio of 1:2:1:5 for **1** and **3**, and Na_2Se, Ga, Ge (Sn), and Se in a molar ratio of 1:2:1:6 for **2** and **4**, were loaded into a graphite crucible and placed in quartz tubes. The tubes were flame-sealed under vacuum (~10^{-4} Torr) and then placed into a temperature controlled muffle furnace, heated from room temperature to 800 ^{o}C in 40 h, kept at that temperature for 96 h, and then cooled to room temperature at 4 °C/h. The products were washed with degassed DMF and dried with ethanol. Yellow crystals of **1** and **2**, orange crystals of **3**, and red crystals of **4**, with respective yields of 60%, 60%, 70%, and 50% based on Ga for **1–4**, were obtained. All the compounds are stable in air and water.

Single-crystal Structure Determination. Block single crystals of **1–4** were selected for single-crystal diffraction. Diffraction data were collected by using graphite monochromated Mo Kα radiation (λ = 0.71073 Å) on a Rigaku Pilatus CCD diffractometer at 293 K. The intensity data sets were collected with a ω-scan technique and reduced using CrystalClear software.[59]

The structures of **1–4** were solved by direct methods and refined by full-matrix least-squares method on F^2 with anisotropic thermal parameters for all atoms. All calculations were performed with SHELXL package of crystallographic software.[60] The formulas collectively consider the crystallographically refined compositions and requirements of charge neutrality. The Addsym/Platon program was used to check the final structures for additional symmetry, and no other missed or higher symmetry element was found.[61] Crystal data and structural refinement information for **1–4** are summarized in Table 1. Atomic coordinates and equivalent isotropic displacement parameters are listed in Table S1. Selected bond distances are reported in Table S2.

Table 1. Crystal data and structure refinement parameters for **1–4**.

	1	**2**	**3**	**4**
Chemical formula	$Na_2Ga_2GeSSe_5$	$Na_2Ga_2GeSe_6$	$Na_2Ga_2SnSSe_5$	$Na_2Ga_2SnSe_6$
Formula weight	684.87	731.77	730.97	777.87
Crystal size (mm^3)	0.117 × 0.115 × 0.106	0.110 × 0.105 × 0.102	0.117 × 0.083 × 0.066	0.071 × 0.063 × 0.046
Crystal system	Orthorhombic			
Space group	*Fdd*2			
a (Å)	12.987(10)	12.985(4)	13.264(4)	13.329(3)
b (Å)	23.653(17)	23.880(8)	23.936(7)	24.291(7)
c (Å)	7.519(5)	7.585(3)	7.514(2)	7.621(2)
V (Å^3)	2310(3)	2352.0(14)	2385.6(12)	2467.5(11)
Z	8	8	8	8
D_{calcd}(g cm^{-3})	3.939	4.133	4.070	4.188
μ(mm^{-1})	23.170	25.671	22.007	24.058
ϑ range (°)	3.25-25.46	3.23-25.46	3.40-25.46	3.19-25.47
GOF on F^2	1.049	0.977	1.114	1.101
$R_1{}^a$ [$I > 2\sigma(I)$]	0.0375	0.0238	0.0257	0.0209
$wR_2{}^b$ [$I > 2\sigma(I)$]	0.0990	0.0486	0.0661	0.0549
$R_1{}^a$ (all data)	0.0389	0.0285	0.0270	0.0218
$wR_2{}^b$(all data)	0.1009	0.0496	0.0668	0.0551
Flack parameter *x*	0.00	0.00	0.00	0.00
$\Delta\rho_{max}/\Delta\rho_{min}$(e Å^{-3})	1.288/-0.991	0.538/-0.986	0.662/-0.768	0.852/-0.528

View Article Online
DOI: 10.1039/C8SC01210E

Powder X-ray Diffraction. Powder X-ray diffraction (PXRD) measurements were performed on a Rigaku MiniFlex II diffractometer using Cu Kα radiation in reflection mode at room temperature with a step size of 0.02° in the range of 2ϑ = 5–65°. The experimental and simulated PXRD patterns of **1–4** are shown in Fig. S2, indicating the purities of the as-synthesized samples, despite the possible existence of a tiny amount of $NaGa_3Se_5$ in phase **2**.

Energy-Dispersive X-ray Spectroscopy Analysis. Semiquantitative microprobe element analyses of the crystals of the four compounds were performed with a field emission scanning electron microscope (FESEM, JSM6700F) equipped with an energy-dispersive X-ray spectroscope (EDX, Oxford INCA). The empirical formula of $Na_{2.3}Ga_{2.1}Ge_{1.0}S_{0.8}Se_{5.1}$ for **1**, $Na_{1.9}Ga_{2.3}Ge_{1.0}Se_{5.8}$ for **2**, $Na_{2.2}Ga_{2.3}Sn_{1.0}S_{1.0}Se_{5.1}$ for **3**, and $Na_{1.8}Ga_{2.0}Sn_{1.0}Se_{6.1}$ for **4** were obtained, and no other element was detected (Fig. S1), which were consistent with the results determined from single-crystal XRD.

SHG Measurements. The SHG measurements of **1–4** were measured using a modified Kurtz-Perry powder technique with 1910 nm laser radiation.[62] Microcrystalline powder samples were ground and sieved into several distinct particle size ranges (30–50, 50–75, 75–100, 100–125, 125–150, and 150–200 μm)for the SHG phase-matching measurements. AGS crystals with similar particle sizes were used as reference. During the measurements, all of the samples were pressed between two glass microscope cover slides and secured in the 1 mm-thick plastic holders. After the mixed signals passed through the monochromator, the doubled frequency signals (955 nm) were detected by an Andor DU420A-BR-DD CCD.

Powder LIDT Measurements. The powder LIDTs of **1–4** and the reference AGS were evaluated by single-pulse measurement method using a focused high-power 1064 nm laser beam with a pulse width τ_p of 10 ns and a repetition rate of 1 Hz.[63] The measurements were conducted by gradually increasing the laser power until the damaged spot of samples was monitored under a microscope after the irradiation. The Nova II sensor with a PE50-DIF-C energy sensor and a vernier caliper were respectively used to measure the power the of laser beam and identify the damaged spots.

Thermal Analyses. The thermal properties of **1–4** were investigated by differential scanning calorimetry (DSC) analysis using a Netzsch STA 449C thermal analyzer in a nitrogen atmosphere. Each sample of approximately 10 mg was placed in sealed silica tubes evacuated to 10^{-4} Torr, heated to 900 °C at 10 °C /min and cooled to 30 °C at 10 °C /min.

Electronic Structure Calculations. Electronic band structures and densities of states (DOS) of **1–4** were calculated using the structure models directly from single-crystal XRD analysis, which are calculated based on density functional theory (DFT) with CASTEP code provided by Materials Studio package.[64-65] The electrons in Na: $2s^22p^63s^1$, Ga: $3d^{10}4s^24p^1$, Ge: $4s^24p^2$, Sn: $5s^25p^2$, S: $3s^23p^4$ and Se: $4s^24p^4$ were treated as valence electrons. The plane-wave cutoff energy is set to 800 eV for **1–4**. Moreover, the numerical integration of the Brillouin zone was performed by using 2 × 1 × 3 Monkhorst–Pack *k*-point meshes for all compounds. The Fermi level (E_f = 0 eV) was selected as reference.

Theoretical studies on optical properties regarding the complex dielectric function $\varepsilon(\omega) = \varepsilon_1(\omega)+i\varepsilon_2(\omega)$ are expressed as follows:[66-67]

$$\varepsilon_2(\omega) = \frac{2e^2\pi}{\Omega\varepsilon_0}\sum_{K,V,C} |< \Psi_K^C |\hat{u}\cdot r| \Psi_K^V >|^2 \delta\left(E_K^C - E_K^V - E\right), \quad (1)$$

where $\delta\left(E_K^C - E_K^V - E\right)$ indicates the energy difference between the conduction and valence bands at *k* point with absorption of energy *E*, $\hat{u}$ denotes the polarization of the incident electric field, Ω is the volume of the primitive cell, *e* is the electric charge, Ψ_K^C and Ψ_K^V are the vectors defining the conduction and valence band wave functions at *k*, respectively, and $\varepsilon_1(\omega)$ can be obtained by using the dispersion relationship of Kramers–Kronig as following:

$$\varepsilon_1(\omega) = 1 + \frac{2}{\pi} P \int_0^\infty \frac{\omega'\varepsilon_2(\omega')}{\omega'^2 - \omega^2} d\omega'. \quad (2)$$

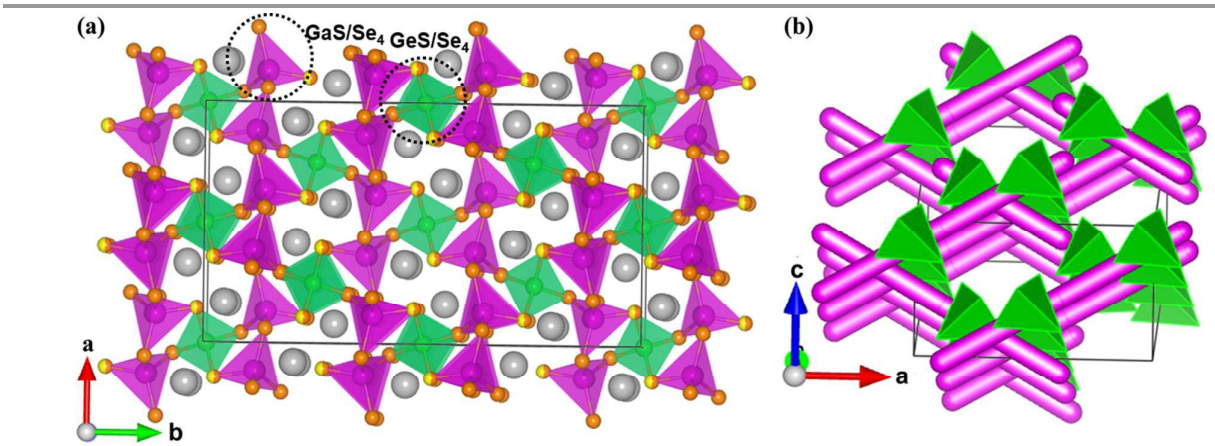

Fig. 1 (a) The 3-D structure of **1** viewed down to the *c* direction. Grey atoms: Na, pink tetrahedra: $[Ga(S/Se)Se_3)]^{5-}$, green tetrahedra: $[Ge(S/Se)_2Se_2]^{4-}$; yellow/orange atoms: S/Se atoms. (b) The infinite $_\infty{}^1[Ga(S/Se)Se_2)]^{3-}$ chains represented as pink columns and isolated $[Ge(S/Se)_2Se_2]^{4-}$ connections (green tetrahedra) in the unit cell of **1**. The Na^+ cations are left out for clarity.

View Article Online
DOI: 10.1039/C8SC01210E

The *P* before the integral indicates the principal value. The first-order nonresonant susceptibility at the low-frequency region is given by $\chi^{(1)}(\omega) = \varepsilon_1(\omega)-1$, and the second-order susceptibilities were calculated using the anharmonic oscillator model.[50]

Results and discussion

Crystal Structure. Compounds **1**~**4** are isostructural and crystallize in the NCS space group of *Fdd*2 in the orthorhombic system with unit cell parameters of *a* = 12.432(4) – 13.329(3) Å, *b* = 22.584(7) – 24.291(7) Å, *c* = 7.239(2) – 7.261(2) Å, and Z = 8. In the asymmetric unit, two crystallographically independent positions are observed for Ga, Ge, or mixed Ga/Sn atoms; three positions for fully occupied S, Se, or mixed S/Se atoms; and one position for Na.

In compound **1**, the 3-D framework consists of two different building blocks, namely, 1D infinite $_\infty^1[Ga(S/Se)Se_2)]^{3-}$ chains (pink tetrahedral chains in Fig. 1a) and isolated $[Ge(S/Se)_2Se_2]^{4-}$ tetrahedra (green tetrahedra in Fig. 1a). Each Ga atom is coordinated by one mixed S/Se and three Se atoms forming the $[Ga(S/Se)Se_3)]^{5-}$ tetrahedra with Ga–S/Se distances ranging from 2.359 Å to 2.406 Å, which then connect with each other by sharing common S/Se atoms to form infinite linear $_\infty^1[Ga(S/Se)Se_2)]^{3-}$ chains. Similar to Ga atoms, each Ge atom is tetrahedrally coordinated by two mixed S/Se and two Se atoms to form the $[Ge(S/Se)_2Se_2]^{4-}$ tetrahedra with Ge–S/Se distances ranging from 2.352 Å to 2.374 Å. These two different building blocks, namely, infinite $_\infty^1[Ga(S/Se)Se_2)]^{3-}$ chains and isolated $[Ge(S/Se)_2Se_2]^{4-}$ tetrahedra, are assembled to form the 3D anionic $(Ga_2GeSSe_5)^{2-}$ framework of **1** (Fig. 1b). Two groups of $_\infty^1[Ga(S/Se)Se_2)]^{3-}$ chains along the *a*+*c* and *a*-*c* directions intersect each other with $[Ge(S/Se)_2Se_2]^{4-}$ tetrahedra acting as the connections between them and forming tunnels along the *c* direction, which are embedded with the counter cations Na^+.

All positions in **2** are fully occupied. In compound **3**, besides the S/Se mixing, the Ga and Sn positions are mixed with a molar ratio of 2:1. The Sn positions in **4**, similar to the Ge positions in **1**, are mixed with Ga with half occupancy. The mixed occupancy of S/Se and Ga/Sn positions are determined by the structural refinements that consider charge balance. The Ga–S(Se), Ge–S(Se), (Ga/Sn)–S, and Na–S(Se) bond lengths in **1–4** (Table S2) are close to those in $BaGa_4S_7$,[25] $BaGa_2GeS_6$,[36] $Ba_2Ga_8GeS_{16}$,[41] $PbGa_2GeSe_6$,[18] $Na_4MgGeSe_6$,[68] $Ba_5Ga_2Se_8$,[69] $KCd_4Ga_5Se_{12}$,[70] $Na_3Mo_{15}Se_{19}$,[71] and $Na_4Sn_3S_8$.[72]

Interestingly, modifying the chalcogen ratio and mutual replacement of Ga, Ge, and Sn atoms does not lead to structural changes in the $Na_2Ga_2MQ_6$ (M = Ge, Sn; Q = S, Se) system. Such structure retention is important when conducting chalcogen or metaldoping to optimize the physical performances of these materials, similar to the case of nonlinear optical materials.[73]

NLO Properties. The SHG of **1–4** has been investigated with a 1910 nm laser and AGS as reference. The SHG signals of **1–4** as a function of particle size are shown in Fig. 2. Their SHG intensities increase with the growth of particle sizes. The results are consistent with type-I phase-matching behavior, which is important in practical applications. Remarkably, the SHG intensities of **1–4** are about 2.3, 1.6, 3.9, and 2.1 times that of commercial AGS with the particle size of 75–100 μm (Fig. 2b). Generally, the SHG signal intensity measured by the Kurtz – Perry powder method is proportional to the square of the second-order NLO coefficient d_{eff}, and the reported d_{eff} of AGS is 12.5 pm/V[26]. Thus, the derived d_{eff} for **1**–**4** are 18.95, 15.81, 24.68, and 18.11 pm/V.

Interestingly, compound **3** $Na_2Ga_2SnSSe_5$ has the highest SHG intensity among these compounds, whereas compound **2** has the lowest. This result is reasonable according to structural analysis. Both S/Se and Ga/Sn occupancy disorders are observed in **3**, which can lead to structural distortion and enhancement of noncentrality and SHG intensity, compared with the corresponding perfect structure. Moreover, the cation size effect may also have effects on the formation of these compounds and ultimately their NLO properties.[74,75]

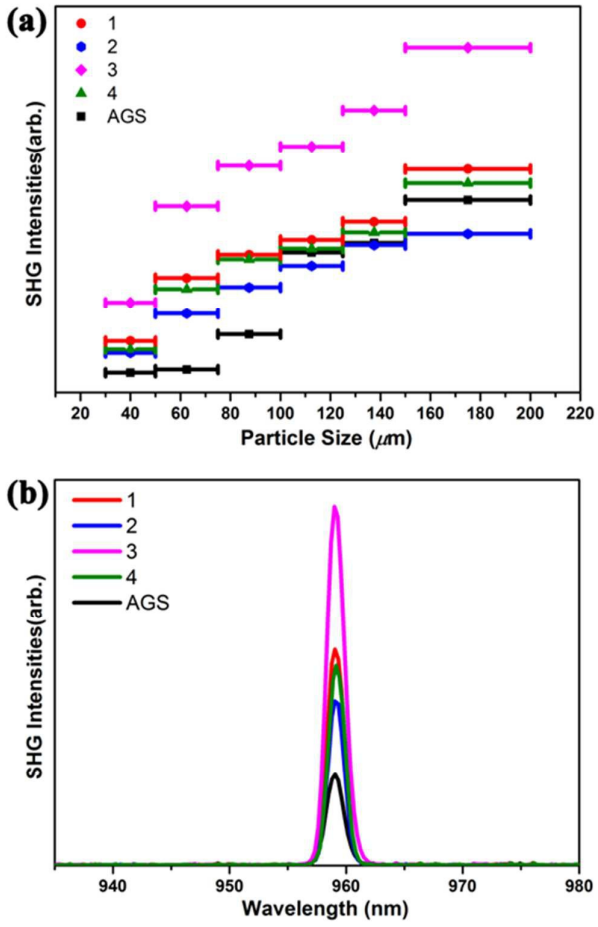

Fig. 2 (a) Phase-matching curves of **1–4** and reference AGS. (b) SHG intensities of **1–4** with AGS as the reference in the particle size of 75–100 μm.

View Article Online
DOI: 10.1039/C8SC01210E

By contrast, no mixing position can be observed in **2,** and no additional SHG enhancement from the structural distortion is present. For cases **1** and **4**, either S/Se (**1**) or Ga/Sn (**4**) is present in their structures, and their SHG intensities are between those of **2** and **3**. Given the structure retention of the $Na_2Ga_2MQ_6$ (M = Ge, Sn; Q = S, Se) system under chalcogen and metal variation, new compounds with SHG intensity even higher than that of **3** may be obtained by the chalcogen and metal variation.

The IR transmission spectra show that compounds **1**–**4** have no obvious intrinsic absorption of chemical bonds in abroad spectral range from 0.25 to 25 μm (Fig. S3), indicating that compounds **1**–**4** may be good candidates for a variety of NLO applications in the mid- and far-IR regions. The optical diffuse reflectance spectra indicate optical band gaps (*E*g) of 1.56, 1.61, 1.63 and 1.73 eV for **1**–**4** (Fig. S4), which are significantly smaller than that of AGS (2.65 eV).[1] The NLO efficiency is positively associated with the band gap, and the band gaps of **1**–**4** narrower than that of AGS are consistent with their NLO efficiencies larger than that of AGS. The band-gap order of *E*g(**1**) < *E*g(**2**) < *E*g(**3**) < *E*g(**4**) is not in accordance with the opposite of NLO efficiency order of d_{eff}(**2**) < d_{eff}(**4**) < d_{eff}(**1**) < d_{eff}(**3**), which can be attributed to the role of structure distortion induced by the atom mixing. Overall, narrowing the band gap of an NLO material is an effective way to achieve large NLO efficiency.

Powder LIDTs. The powder LIDTs of **1**–**4** and the benchmark AGS measured by the single pulse method is summarized in Table 2. During the measurement, small spot areas with size of 0.1590, 0.1662, 0.2463 and 0.1963 cm^2 are selected for **1**–**4**, respectively. The measured damage energies of **1–4** (20.07–27.99 mJ) are much higher than that of AGS (11.02 mJ). The derived powder LIDTs of **1**–**4** are 9.9, 13.3, 8.5, and 10.1 times that of AGS, supporting their potential for high-power applications. In this study, the experimental LIDT of benchmark AGS is 1.27 $MW{\cdot}cm^{-2}$, which is close to the reported values.[18] According to the conventional view of incompatibility between large NLO efficiency and high LIDT NLO materials, compounds **1**–**4** with band gaps of significantly narrower than that of AGS should have smaller LIDT.

However, the experimental LIDT values of **1**–**4** are much higher than that of AGS, and there should be other factors that dominate the LIDT of **1**–**4**, rather than the band gap, although the LIDT order of LIDT (**3**) < LIDT (**1**) < LIDT (**4**) < LIDT (**2**) is in accordance with the opposite of NLO efficiency order of d_{eff}(**2**) < d_{eff}(**4**) < d_{eff}(**1**) < d_{eff}(**3**). This issue is discussed in the following section.

Table 2. LIDTs of **1~4**.

Compound	Damage Energy (mJ)	Spot Area (cm^2)	Damage Threshold [$MW{\cdot}cm^{-2}$]
1	20.07	0.1590	12.62
2	27.99	0.1662	16.84
3	26.59	0.2463	10.79
4	25.19	0.1963	12.82
AGS	11.02	0.8659	1.27

Table 3. Thermal expansion coefficients α_L ($\times 10^{-5}$ K^{-1}) of *a*, *b* and *c* axis lengths and thermal expansion anisotropy of **1–4** and reference AGS.

	1	**2**	**3**	**4**	**AGS**
a	5.58	5.86	-5.46	3.68	3.08
b	-5.54	6.85	-2.71	-4.09	3.08
c	-8.81	-8.75	2.99	5.52	-9.158
δ	1.59	1.49	2.01	1.51	2.97

Thermal Properties. Thermal effects are non-negligible in the practical application of mid-IR NLO materials; the large temperature increase caused by optical absorptions lead to thermal expansion, strain, distortion, cracking, catastrophic shattering, and damage of crystals.[51] Thermal expansion anisotropy (TEA, δ) of NLO materials is identified as one of the most important intrinsic parameters that influence the ultimate experimental derived LIDTs. NLO materials with smaller TEA tend to sustain a larger thermal shock under laser irradiation and exhibit higher LIDTs. To study the TEA of **1–4** and the reference AGS, the temperature dependence of the lattice parameters was measured using an X-ray diffractometer from 300 K to 500 K with a step of ~20 K (Fig. S6). The thermal expansion coefficients (TEC, $\alpha_L = R_0^{-1}[dR(T)/dT]$, R_0 is the value at T = 0 K) of the lattice parameters (*a*, *b*, *c* axis lengths) of **1~4** are derived. TEA (δ), defined as the ratio of the maximum and minimum of TECs, are 1.59, 1.49, 2.01 and 1.51 for **1–4** (Table 3). The TEC and TEA of AGS have been measured in our previous work[76] and are close to the other reported values.[77]

The measured TEA order of δ(AGS) > δ(**3**) > δ(**1**) > δ(**4**) > δ(**2**) is in accordance with their experimental LIDTs that have the opposite order. According to the structural analysis of the four compounds, atom mixing occurs in the structures except **2**, where the structural defects are indispensable, as well as the defect-induced optical absorptions during the measurements. TEA is proposed to be the dominant factor of LIDTs of the $Na_2Ga_2MQ_6$ (M = Ge, Sn; Q = S, Se) system, as supported by the experimental results. Reducing the thermal effect, especially by decreasing the thermal expansion anisotropy of an NLO material, is reasonable to achieve high LIDT. The TEA and LIDT of some typical IR NLO crystals, $LiInS_2$, $ZnGeP_2$, GaSe and $AgGaSe_2$ have been listed in Table S3. The TEA of $ZnGeP_2$ and GaSe are close to each other, resulting in their similar LIDTs. The TEA of $LiInS_2$ is much larger than that of AGS. However, its LIDT is also much larger than that of AGS, which can be ascribed to the shorter pulse width used for the LIDT measurement of $LiInS_2$.

The DSC results in Fig. S5 show that compounds **1–4**

View Article Online
DOI: 10.1039/C8SC01210E

undergo congruent melting upon heating and crystallization upon cooling events with relatively lower melting temperatures (606, 571, 659, and 689 °C for **1–4**). In comparison, the melting points of the known IR NLO materials, such as AGS (998 °C), $LiGaS_2$ (1050 °C), $LiGaSe_2$ (915 °C), $BaGa_4S_7$ (1090 °C), and $BaGa_4Se_7$ (968 °C) [40] are significantly higher. These results reveal that large crystals of **1–4** can be grown using the Bridgman method at lower temperatures.

Theoretical Calculations. Theoretical band gaps of **1–4** are calculated to be 2.01, 2.02, 2.00, and 1.95 eV, (Fig. S7). Compared with the experimental results, the calculated band gaps of **1–4** have certain deviations due to the limitation of the DFT method in semiconductors and insulators.[78-79] As observed seen from the partial DOS presented in Fig. S8, for all four compounds, the valence band close to the Fermi level originates predominantly from Se-4p and S-3p states for **1**, **3** and Se-4p for **2**, **4**. The conductive bands (CB) of **1–4** close to the CB bottom are mostly composed of Ga-4p, Ge-4p and Se-4p states in **1**, Ge-4p and Se-4s states in **2**, and Sn-5p and Se-4s states in **3** and **4**. Therefore, their optical absorptions can be mainly attributed to the charge transfer from Se-4p (S-3p) states to Sn-5p (Ga-4p, Ge-4p) and Se-4p (Se-4s) states, and the electronic structure around the band edges is mainly derived from the $(Sn/Ga/Ge)(S/Se)_4$ tetrahedra units, which provide the dominant states in the optical matrix elements describing the virtual excitations of the SHG effect in **1–4**. The strongly isolated s and p orbitals of Na^+ cations are localized far from the band gaps and have a negligible influence on the SHG effect.

To obtain a profound understanding of the NLO properties of **1–4**, the theoretical calculations of SHG coefficients were performed. The real (ε_1) and imaginary (ε_2) parts of optical dielectric constants along the *x*, *y* and *z* directions are shown in Fig. S9 and S10. The curves of ε_2^{ave}, defined as $(\varepsilon_x+\varepsilon_y+\varepsilon_z)/3$, reveal the strongest absorptions of **1** at 5.72, **2** at 5.54, **3** at 8.54, and **4** at 8.74 eV, which can be mainly assigned to the electronic interband transitions according to the DOS analysis. Owing to the NCS point group of *mm*2, compounds **1–4** have three independent non-zero SHG tensors d_{113}, d_{223}, and d_{333} under the restriction of Kleinman symmetry.The calculated energy dependence of SHG tensors of **1–4** are shown in Fig. 3, at the wavelength of 1910 nm (0.6492 eV). The d_{113}, d_{223}, and d_{333} values are 18.72, 19.22 and 19.09 pm/V for **1**; 13.89, 13.39 and 13.84 pm/V for **2**; 23.69, 22.10 and 22.28 pm/V for **3**; and 17.06, 16.83 and 16.21 pm/V for **4**. The calculated average SHG coefficients d_{cal} defined as the arithmetic mean of all SHG tensors with a descending order of d_{cal}(**3**, 22.69 pm/V) > d_{cal}(**1**, 19.01 pm/V) > d_{cal}(**4**, 16.70 pm/V) > d_{cal}(**2**, 13.71 pm/V) are consistent with the experimental results.

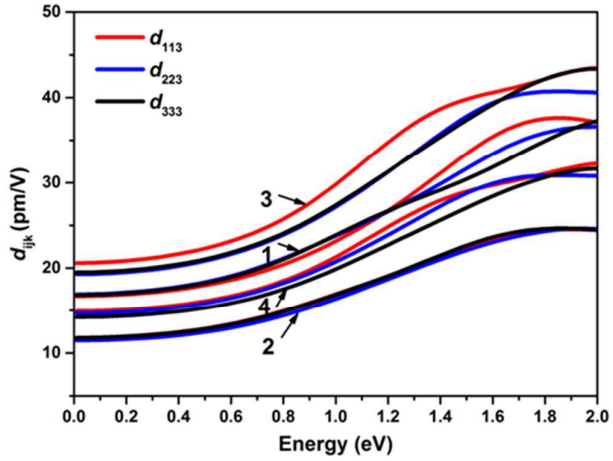

Fig. 3 Calculated frequency-dependent SHG coefficients of **1–4**.

Conclusions

A new strategy to circumvent the incompatibility between the large NLO efficiency and high LIDT in mid-infrared NLO materials, namely, narrowing band gap for large NLO efficiency and reducing thermal effect for high LIDT, is proposed in this study. To support this proposal, a series of isostructural chalcogenides with different tetrahedral center cations, $Na_2Ga_2MQ_6$ (M = Ge, Sn; Q = S, Se), were successfully synthesized using the solid-state method. The 3D structures of these chalcogenides were assembled by 1D infinite $_\infty^1[Ga(Sn)Q_3)]^{3-}$ tetrahedral chains and $[MQ_4]^{4-}$ tetrahedral connections. All of them exhibit large SHG responses of approximately 1.6–3.9 × AGS with phase-matching ability, which result from their relatively small band gaps (1.56–1.73 eV) compared with AGS (2.65 eV). They also exhibit outstanding LIDTs of 8.5–13.3 × AGS for potential high-power applications, which is contrary to the conventional view on band gaps. However, the measured thermal expansion anisotropy order of these compounds is in agreement with their experimental LIDTs with the opposite order, indicating that thermal expansion anisotropy is one of the main thermal parameters that influence LIDTs of IR NLO materials and high LIDT can be achieved by reducing the thermal effect. The results of this study shed light on the exploration of practical IR NLO materials with excellent performances not restricted by the NLO–LIDT incompatibility.

Conflicts of interest

There are no conflicts to declare.

Acknowledgements

This work was financially supported by the NSF of China (21701176), the National Postdoctoral Program for Innovative Talents (BX201600163), the China Postdoctoral Science Foundation (2016M600510), the National Key Laboratory Development Fund (20180026) and the NSF of Fujian Province (2018J05034).

Notes and references

View Article Online
DOI: 10.1039/C8SC01210E

1 L. Kang, M. Zhou, J. Yao, Z. Lin, Y. Wu, and C. Chen, *J. Am. Chem. Soc.*, *2015*, **137**, 13049.
2 H. Zhang, M. Zhang, S. Pan, X. Dong, Z. Yang, X. Hou, Z. Wang, K. B. Chang, and K. R. Poeppelmeier, *J. Am. Chem. Soc.*, 2015, **137**, 8360.
3 H. Yu, J. Young, H. Wu, W. Zhang, J. M. Rondinelli, and P. S. Halasyamani, *J. Am. Chem. Soc*., 2016, **138**, 4984.
4 I. Chung, and M. G. Kanatzidis, *Chem. Mater.* 2014, **26**, 849.
5 C. Chen, *Sci. Sin. Ser. B*, 1985, **28**, 235.
6 C. Chen, Y. Wu, A. Jiang, B. Wu, G. You, R. Li, and S. Lin, *J. Opt. Soc. Am. B*, 1989, **6**, 616.
7 V. G. Dmitriev, G. G. Gurzadyan, and D. N. Nikogosyan, Handbook of nonlinear optical crystals; Springer-Verlag, New York, 1999.
8 C. Chen, Y. Wang, B. Wu, K. Wu, W. Zeng, and L. Yu, *Nature*, 1995, **373**, 322.
9 T. A. Driscoll, P. E. Perkins, H. J. Hoffman, and R. E. Stone, *J. Opt. Soc. Am. B*, 1986, **3**, 683.
10 T. K. Bera, J. I. Jang, J. B. Ketterson, and M. G. Kanatzidis, *J. Am. Chem. Soc*., 2008, **131**, 75.
11 I. Chung, and M. G. Kanatzidis, *Chem. Mater*., 2013, **26**, 849.
12 F. Liang, L. Kang, Z. Lin, and Y. Wu, *Cryst. Growth Des.*, 2017, **17**, 2254.
13 A. Harasaki, and K. Kato, *J. Jpn. Appl. Phys.*, 1997, **36**, 700.
14 A. Jayaraman, V. Narayanamurti, H. Kasper, M.Chin, and R. Maines, *Phy. Rev. B*, 1976, **14**, 3516.
15 G. Catella, L. Shiozawa, J. Hietanen, R. Eckardt, R. Route, R. Feigelson, D. Cooper, and C. Marquardt, *Appl. Opt.*, 1993, **32**, 3948.
16 M. C. Ohmer, R. Pandey, *MRS Bulletin*, **1998**, *23*, 16–22.
17 G. Boyd, E. Buehler, and F. Storz, *Appl. Phy. Lett.*, 1971, **18**, 301.
18 Z. Z. Luo, C. S. Lin, H. H. Cui, W. L. Zhang, H. Zhang, H. Chen, Z. Z. He, and W. D. Cheng, *Chem. Mater*., 2015, **27**, 914.
19 G. Li, K. Wu, Q. Liu, Z. Yang, and S. Pan, *J. Am. Chem. Soc.*, 2016, **138**, 7422.
20 K. Wu, Z. Yang, and S. Pan, *Chem. Mater*., 2016, **28**, 2795.
21 A. P. Yelisseyev, L. I. Isaenko, P. Krinitsin, F. Liang, A. A. Goloshumova, D. Y. Naumov, and Z. Lin, *Inorg. Chem.*, 2016, **55**, 8672.
22 S. Fossier, S. Salaün, J. Mangin, O. Bidault, I. Thénot, J.-J. Zondy, W. Chen, F. Rotermund, V. Petrov, P. Petrov, J. Henningsen, A. Yelisseyev, L. Isaenko, S. Lobanov, O. Balachninaite, G. Slekys, and V. Sirutkaitis, *J. Opt. Soc. Am. B*, 2004, **21**, 1981.
23 V. Petrov, J. J. Zondy, O. Bidault, L. Isaenko, V. Vedenyapin, A. Yelisseyev, W. Chen, A. Tyazhev, S. Lobanov, G. Marchev, *J. Opt. Soc. Am. B*, 2010, **27**, 1902.
24 L. Isaenko, A. Yelisseyev, S. Lobanov, P. Krinitsin, V. Petrov, and J. J. Zondy, *J. Non-Cryst. Solids.,* 2006, **352**, 2439.
25 X. Lin, G. Zhang, and N. Ye, *Cryst. Growth Des.,* 2008, **9**, 1186.
26 J. J. Zondy, D. Touahri, and O. Acef, *J. Opt. Soc. Am. B*, 1997, **14**, 2481.
27 V. Petrov, A. Yelisseyev, L. Isaenko, S. Lobanov, A. Titov, and J. J. Zondy, *Applied Physics B*, 2004, **78**, 543.
28 G. A. Marking, J. A. Hanko, and M. G. Kanatzidis, *Chem. Mater*., 1998, **10**, 1191.
29 T. V. Misuryaev, T. V. Murzina, O. A. Aktsipetrov, N. E. Sherstyuk, V. B. Cajipe, and X. Bourdon, *Solid State Commun*., 2000, **115**, 605.
30 J. H. Liao, G. Marking, K. Hsu, Y. Matsushita, M. Ewbank, R. Borwick, P. Cunningham, M. Rosker, and M. Kanatzidis, *J. Am. Chem. Soc.*, 2003, **125**, 9484.
31 J. W. Lekse, M. A. Moreau, K. L. McNerny, J. Yeon, P. S. Halasyamani, and J. A. Aitken, *Inorg. Chem*., 2009, **48**, 7516.
32 L. Geng, W. D. Cheng, C. S. Lin, W. L. Zhang, H. Zhang, and Z. Z. He, *Inorg. Chem.*, 2011, **50**, 5679.
33 D. Mei, W. Yin, K. Feng, Z. Lin, L. Bai, J. Yao, and Y. Wu, *Inorg. Chem.*, 2011, **51**, 1035.
34 H. Lin, L. J. Zhou, and L. Chen, *Chem. Mater.*, 2012, **24**, 3406.
35 D. Mei, W. Yin, K. Feng, Z. Lin, L. Bai, J. Yao, and Y. Wu, *Inorg. Chem*., 2012, **51**, 1035.
36 W. Yin, K. Feng, R. He, D. Mei, Z. Lin, J. Yao, and Y. Wu, *Dalton Trans.*, 2012, **41**, 5653.
37 J. I. Jang, S. Park, C. M. Harrison, D. J. Clark, C. D. Morris, I. Chung, and M. G. Kanatzidis, *Opt. lett*., 2013, **38**, 1316.
38 S. M. Kuo, Y. M. Chang, I. Chung, J. I. Jang, B. H. Her, S. H. Yang, J. B. Ketterson, M. G. Kanatzidis, and K. F. Hsu, *Chem. Mater.*, 2013, **25**, 2427.
39 J. A.Brant, D. J. Clark, Y. S. Kim, J. I. Jang, J.-H. Zhang, and J. A. Aitken, *Chem. Mater*., 2014, **26**, 3045.
40 X. Li, C. Li, P. Gong, Z. Lin, J. Yao, and Y. Wu, *J. Mater. Chem. C*, 2015, **3**, 10998.
41 B. W. Liu, H. Y. Zeng, M. J. Zhang, Y. H. Fan, G. C. Guo, J. S. Huang, and Z. C. Dong, *Inorg. Chem*., 2015, **54**, 976.
42 B. W. Liu, H. Y. Zeng, X. M. Jiang, G. E. Wang, S. F. Li, L. Xu, and G. C. Guo, *Chem. Sci.*, 2016, **7**, 6273.
43 K. Wu, Z. Yang, and S. Pan, *Angew. Chem. Int. Ed.*, 2016, **55**, 6713.
44 K. Wu, Z. Yang, and S. Pan, *Chem. Commun.*, 2017, **53**, 3010.
45 S. Das, C. Ghosh, S. Gangopadhyay, Y. M. Andreev, and V. V. Badikov, *J. Jpn. Appl. Phys*., 2006, **45**, 5795.
46 O. M. Yurchenko, I. D.Olekseyuk, and O. V. Parasyuk, *J. of Cryst. Growth*, 2005, **275**, e1983.
47 V. Petrov, V. Badikov, G. Shevyrdyaeva, V. Panyutin, and V. Chizhikov, *Opt. Mater.*, 2004, **26**, 217.
48 W. Yin, K. Feng, W. Hao, J. Yao, and Y. Wu, *Inorg. Chem.*, 2012, **51**, 5839.
49 Y. Kim, I. S. Seo, S. W. Martin, and J. Baek, *Chem. Mater.*, 2008, **20**, 6048.
50 R. W. Boyd, *Nonlinear optics*. Academic press: **2003**.
51 D. Ristau, Laser-induced damage in optical materials. CRC Press: **2014**.
52 G. C. Guo, Y. Yao, K. Wu, L. Wu, and J. Huang, *Prog. Chem.,* 2001, **13**, 151.
53 S. P. Guo, Y. C., and G. C. Guo, *Chem. Rev.*, 2017, **335**, 44.
54 B. W. Liu, M. Y. Zhang, X. M. Jiang, S. F. Li, H. Y. Zeng, G. Q. Wang, Y. H. Fan, Y. F. Su, C. Li, G. C. Guo, and J. S. Huang. *Chem. Mater.*, 2017, **29**, 9200.
55 I. D. Brown, *Struct Bond,* 2014, **158**, 11.
56 C. D. Morris, I. Chung, S. Park, C. M. Harrison, D. J. Clark, J. I. Jang, and M. G. Kanatzidis, *J. Am. Chem. Soc.*, 2012, **134**, 20733.
57 I. Chung, J.-H. Song, J. I. Jang, A. J. Freeman, and M. G. Kanatzidis, *J. Solid State Chem*., 2012, **195**, 161.
58 A. S. Haynes, F. O. Saouma, C. O. Otieno, D. J. Clark, D. P. Shoemaker, J. I. Jang, and M. G. Kanatzidis, *Chem. Mater.,* 2015, **27**, 1837.
59 Rigaku *CrystalClear*, 1.3.5; Rigaku Corp., Tokyo: **2002**.
60 G.Sheldrick, SHELXS-97, program for X-ray crystal structure solution. University of Göttingen, Germany: **1997**.
61 A. Spek, Single-crystal structure validation with the program PLATON. *Journal of Applied Crystallography* **2003**, *36*, 7–13.
62 S. Kurtz, and T. *J.* Perry, *Appl. Phys.*, 1968, **39**, 3798.
63 M. J. Zhang, X. M. Jiang, L. J. Zhou, and G. C. Guo, *J. Mater. Chem. C*, 2013, **1**, 4754.
64 M. C. Payne, M. P. Teter, D. C. Allan, T. A. Arias, and J. D. Joannopoulos, *Rev. Mod. Phys.*, 1992, **64**, 1045.
65 S. J. Clark, M. D. Segall, C. J. Pickard, P. J. Hasnip, M. I. Probert, K. Refson, and M. C. Payne, *Z. Kristallogr.*, 2005, **220**, 567.
66 F. P. Bassani, G. P., *Electronic States and Optical Transitions in Solids*. Pergamon Press Ltd.: Oxford, 1975; p149–154.
67 M. Gajdoš, K. Hummer, G. Kresse, J. Furthmüller, and F. Bechstedt, *Phys. Rev. B*, 2006, **73**, 045112-1.

View Article Online
DOI: 10.1039/C8SC01210E

68 K. Wu, Z. Yang, and S. Pan, *Inorg. Chem.*, 2015, **54**, 10108.
69 D. Mei, W. Yin, Z. Lin, R. He, J. Yao, P. Fu, and Y. Wu, *J. Alloy. Compd.*, 2011, **509**, 2981.
70 H. Lin, L. Chen, L. J. Zhou, and L. M. Wu, *J. Am. Chem. Soc.*, 2013, **135**, 12914.
71 J. Tarascon, G. Hull, and J. Waszczak, *Mater. Res. Bull.*, 1985, **20**, 935.
72 J. C. Jumas, E. Philippot, and M. Maurin, *J. Solid State Chem.*, 1975, **14**, 152.
73 A. Rothenberger, H. H. Wang, D.Chung, and M. G. Kanatzidis, I*norg. Chem.*, 2010, **49**, 1144.
74 K. M. Ok, *Acc. Chem. Res.*, 2016, **49**, 2774.
75 H. Jo, S.-J. Oh, and K. M. Ok, *Dalton Trans.*, 2017, **46**, 15628.
76 S. F. Li, X. M. Jiang, B. W. Liu, D. Yan, C. S. Lin, H. Y. Zeng, and G. C. Guo, *Chem. Mater.*, 2017, **29**, 1796.
77 I. Bodnar, and N. Orlova, *Phys. stat. sol. (a)*, 1985, **91**, 50.
78 J. P. Perdew, and M. Levy, *Phys. Rev. Lett*., 1983, **51**, 1884.
79 J. P. Perdew, J. A. Chevary, S. H. Vosko, K. A. Jackson, M. R. Pederson, D. J. Singh, and C. Fiolhais, *Phy. Rev. B*, 1992, **46**, 6671.

View Article Online
DOI: 10.1039/C8SC01210E

New Strategy for Designing Promising Mid-Infrared Nonlinear Optical Materials: Narrowing Band Gap for Large Nonlinear Optical Efficiency and Reducing Thermal Effect for High Laser-induced Damage Threshold

Shu-Fang Li,[a] Xiao-Ming Jiang,[a,*] Yu-Hang Fan,[b] Bin-Wen Liu,[a] Hui-Yi Zeng,[a] and Guo-Cong Guo[a,*]

Graphic Abstract

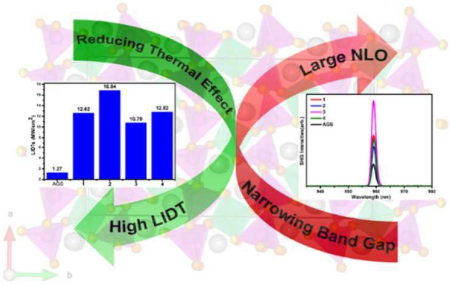

A new strategy is verified on the exploration of practical IR NLO materials not restricted by the NLO–LIDT incompatibility.